

See discussions, stats, and author profiles for this publication at: <https://www.researchgate.net/publication/49825092>

Dynamic Hydrogen-Bonding Network in the Distal Pocket of the Nitrosyl Complex of *Pseudomonas aeruginosa* cd(1) Nitrite Reductase

ARTICLE in JOURNAL OF THE AMERICAN CHEMICAL SOCIETY · FEBRUARY 2011

Impact Factor: 12.11 · DOI: 10.1021/ja109688w · Source: PubMed

CITATIONS

16

READS

41

6 AUTHORS, INCLUDING:



Marina Radoul

Weizmann Institute of Science

6 PUBLICATIONS 124 CITATIONS

SEE PROFILE



D. A. Bykov

Aarhus University

13 PUBLICATIONS 85 CITATIONS

SEE PROFILE



Serena Rinaldo

Sapienza University of Rome

46 PUBLICATIONS 423 CITATIONS

SEE PROFILE



Francesca Cutruzzola

Sapienza University of Rome

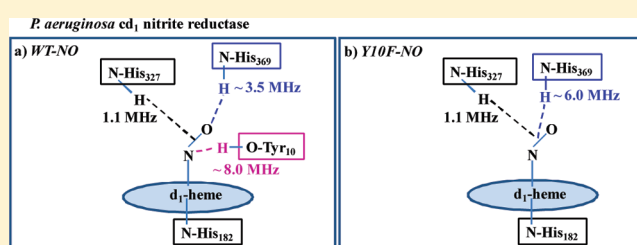
126 PUBLICATIONS 2,182 CITATIONS

SEE PROFILE

Dynamic Hydrogen-Bonding Network in the Distal Pocket of the Nitrosyl Complex of *Pseudomonas aeruginosa* cd₁ Nitrite ReductaseMarina Radoul,[†] Dmytro Bykov,[‡] Serena Rinaldo,[§] Francesca Cutruzzolà,[§] Frank Neese,^{*,‡} and Daniella Goldfarb^{*,†}[†]Department of Chemical Physics, Weizmann Institute of Science, Rehovot 76100, Israel[‡]Institute for Physical and Theoretical Chemistry, University of Bonn, Wegelerstrasse 12, Bonn -53115, Germany[§]Dipartimento di Scienze Biochimiche "A. Rossi Fanelli", Università di Roma "La Sapienza", Rome, Italy

S Supporting Information

ABSTRACT: cd₁ nitrite reductase (NIR) is a key enzyme in the denitrification process that reduces nitrite to nitric oxide (NO). It contains a specialized d₁-heme cofactor, found only in this class of enzymes, where the substrate, nitrite, binds and is converted to NO. For a long time, it was believed that NO must be released from the ferric d₁-heme to avoid enzyme inhibition by the formation of ferrous–nitroso complex, which was considered as a dead-end product. However, recently an enhanced rate of NO dissociation from the ferrous form, not observed in standard b-type hemes, has been reported and attributed to the unique d₁-heme structure (Rinaldo, S.; Arcovito, A.; Brunori, M.; Cutruzzolà, F. *J. Biol. Chem.* **2007**, *282*, 14761–14767). Here, we report on a detailed study of the spatial and electronic structure of the ferrous d₁-heme NO complex from *Pseudomonas aeruginosa* cd₁ NIR and two mutants Y10F and H369A/H327A in solution, searching for the unique properties that are responsible for the relatively fast release. There are three residues at the “distal” side of the heme (Tyr₁₀, His₃₂₇, and His₃₆₉), and in this work we focus on the identification and characterization of possible H-bonds they can form with the NO, thereby affecting the stability of the complex. For this purpose, we have used high field pulse electron–nuclear double resonance (ENDOR) combined with density functional theory (DFT) calculations. The DFT calculations were essential for assigning and interpreting the ENDOR spectra in terms of geometric structure. We have shown that the NO in the nitrosyl d₁-heme complex of cd₁ NIR forms H-bonds with Tyr₁₀ and His₃₆₉, whereas the second conserved histidine, His₃₂₇, appears to be less involved in NO H-bonding. This is in contrast to the crystal structure that shows that Tyr₁₀ is removed from the NO. We have also observed a larger solvent accessibility to the distal pocket in the mutants as compared to the wild-type. Moreover, it was shown that the H-bonding network within the active site is dynamic and that a change in the protonation state of one of the residues does affect the strength and position of the H-bonds formed by the others. In the Y10F mutant, His₃₆₉ is closer to the NO, whereas mutation of both distal histidines displaces Tyr₁₀, removing its H-bond. The implications of the H-bonding network found in terms of the complex stability and catalysis are discussed.



■ INTRODUCTION

The denitrifying enzyme cd₁ nitrite reductase (cd₁ NIR) catalyzes the reduction of nitrite (NO₂[−]) to nitric oxide (NO) as a part of the denitrification process.^{1,2} The cd₁ NIR purified from the periplasm of the denitrifying bacteria *Pseudomonas aeruginosa* (*P. aeruginosa*) is a homodimer, each monomer of the enzyme contains one c-heme and one unique d₁-heme.^{3–5} The c-heme accepts electrons from external electron donors⁶ and transfers them to the d₁-heme, where nitrite binds and is converted to NO.^{3,6,7} In the past, the d₁ Fe(II)–NO bound state of cd₁ NIR has been considered as a “dead end” product, and therefore it was believed that the NO release must take place from the Fe(III)–NO state.^{8,9} However, a recent kinetic study¹⁰ on *P. aeruginosa* cd₁ NIR has shown, unexpectedly, that NO can be rather rapidly released from the fully reduced d₁-heme despite its high affinity (*K*_d ≈ 10⁷ M) for the heme Fe(II). The NO dissociation rate of

P. aeruginosa cd₁ NIR is ~70 s^{−1}, which is 100-fold faster than that measured for any other heme in the ferrous state.¹⁰ These new findings reveal the uniqueness of the behavior of cd₁ NIR among other hemoproteins.^{11–13} On the basis of these studies, it was proposed that the unique d₁-heme structure might be a prerequisite for the faster rate of NO dissociation from the ferrous form, a property that cannot be achieved with a standard b-type heme.¹⁴ The catalytic activity of *P. aeruginosa* cd₁ NIR therefore depends on the unique chemical structure of the d₁-heme. An important role is also played by the two conserved histidines (His₃₂₇ and His₃₆₉), located in the active site pocket.^{10,15,16} Interestingly, a relatively fast NO dissociation

Received: October 28, 2010

Published: February 10, 2011

rate has been observed also for the H369A mutant (where His₃₆₉ is replaced by alanine).¹⁰

The three-dimensional (3D) crystal structures of *P. aeruginosa* cd₁ NIR of the wild-type (WT) in the oxidized (pdb 1nir),¹⁵ reduced, and reduced-NO bound (pdb 1nno)⁷ states have been determined. A distinctive feature of *P. aeruginosa* cd₁ NIR enzyme is the so-called “domain swapping” of its N-terminal tail that brings tyrosine (Tyr₁₀) of one monomer close to the d₁-heme site of the other monomer. Tyr₁₀ is hydrogen bonded to the hydroxide axial ligand of the oxidized d₁-heme. The reduced and NO-bound WT *P. aeruginosa* cd₁ NIR structures were obtained by soaking the crystals of the oxidized protein with sodium ascorbate and potassium nitrite.⁷ Reduction of the WT *P. aeruginosa* cd₁ NIR was found to lead to conformational changes⁷ involving tightening of the 56–62 loop in the c-heme domain and rotation of the Tyr₁₀ side chain resulting in a 4.2 Å shift of the tyrosine OH group. This movement opens the active site pocket, giving access to the substrate. In the Fe(II) NO-bound state, the Fe–N–O angle was found to be 135°, and the two conserved histidines were found within hydrogen-bond distance to the oxygen of NO (3.4 Å to His₃₂₇ and 2.6 Å to His₃₆₉). Tyr₁₀ is shifted away, with a distance of 4.9 and 4.1 Å between its O(OH) and the nitrogen and oxygen of the NO, respectively.

The location of His₃₂₇, His₃₆₉, and Tyr₁₀ in the d₁-heme pocket and the formation of H-bonds between these residues and the substrate (NO₂[−]) and the product (NO) are strategic factors in catalysis. The H327A and H369A mutants of *P. aeruginosa* cd₁ NIR showed a 100-fold decrease in the nitrite reductase activity as compared to the WT.¹⁶ It was also found that the contribution of the two histidines is not equivalent; the H369A mutant showed a more significant decrease in the affinity for nitrite. On the other hand, no effect on the nitrite reductase activity was reported for the Y10F mutant.¹⁷ The nitrosyl complexes of the H327A (pdb 1hzu) and H369A (pdb 1hzu) mutants^{16,18} showed significant differences with respect to the nitrosyl complexes of the WT. The N-terminal region of the H327A and H369A mutants is disordered, and therefore it is difficult to ascertain whether Tyr₁₀ is located in the vicinity of the d₁-heme distal pocket; the d₁-heme of both mutants is remarkably more accessible to the solvent than the WT enzyme.¹⁷ In the H369A–NO complex, the position and orientation of the NO is significantly different from that of the NO bound to the reduced WT structure. Moreover, in this mutant, NO is within H-bonding distance to a water molecule, which replaces His₃₆₉ (2.7 Å). These studies demonstrate the structural flexibility of the active site of the cd₁ NIR¹⁷ and raise the questions of whether the structural changes observed in the crystal take place also in solution and whether they are relevant for the activity of the enzyme.

To date, a direct observation and characterization of the proposed hydrogen bonds in the distal active site pocket of the nitrosyl d₁-heme in solution have not been reported. These may play a role in the stabilization/destabilization of the NO bound state. Here, we present a detailed study of the distal heme pocket of the nitrosyl d₁-heme complex focusing on the hydrogen bonding to the NO. Specifically, we have investigated the nitrosyl complexes of WT, Y10F, and dHis (a double mutant H327A/H369A, where both His₃₂₇ and His₃₆₉ were replaced by alanines) by a combination of high field electron–nuclear double resonance (ENDOR) techniques (W-band, 95 GHz) and density function theory (DFT) calculations. ENDOR spectra yield the hyperfine interactions of the unpaired electron with magnetic nuclei in its close vicinity, and their analysis gives structural

information. Relating the hyperfine couplings to structural parameters is often nontrivial and requires quantum chemical calculations.^{19–21} Here, DFT calculations were required for both signal assignment and interpretation of the spin Hamiltonian parameters in terms of structure because of the overlapping ENDOR signals of several H-bonds. We have recently demonstrated the effectiveness of this approach in the investigation of the H-bond characteristics of the nitrosyl complex of myoglobin (Mb–NO),²² which serves as an excellent reference for the present work.

The well resolved *g*-anisotropy of the nitrosyl d₁-heme complex at W-band (95 GHz, 3.5 T) allows one to perform orientation selective measurements essential for unique determination of the hyperfine and quadrupole interactions of the ¹H/²H nuclei participating in H-bonding. DFT calculations were carried out on a number of optimized structures varying in the protonation states of the two histidines, which are not provided by the X-ray measurements, and the relevant EPR parameters were calculated for each structure. These were compared to the experimental results, and the degree of the agreement between the experiments and calculations was used as the basis for the assignment of the experimentally detected H-bonds. This also provided insight into conformational changes that may be induced by protonation/deprotonation of the histidines. Two H-bonds to the NO were found in WT and assigned to Tyr₁₀ and His₃₆₉. Protonation of N^ε of His₃₆₉ holds Tyr₁₀ in place for forming an H-bond with the NO, and its deprotonation leads to an H-bond of Tyr₁₀ with the N^ε removing the H-bond with the NO. In the Y10F mutant, His₃₆₉ is closer to the NO and its hydrogen bond shorter, whereas mutation of both distal histidines displaces Tyr₁₀, removing its H-bond with the NO. Finally, a larger solvent accessibility into the distal pocket of the mutants as compared to WT was found.

■ EXPERIMENTAL SECTION

Mutagenesis and Protein Purification. WT *Pseudomonas aeruginosa* cd₁ NIR was purified as described elsewhere.²³ Mutagenesis, expression in *Pseudomonas putida*, and purification of the Y10F and dHis were performed as described earlier.^{17,24,25} Because the *Pseudomonas putida* expression system could not produce the protein that contains the d₁-heme, but only the c-heme, this semiapo-NIR was reconstituted in vitro with the d₁-heme extracted from WT *P. aeruginosa* cd₁ NIR as detailed elsewhere.²²

Sample Preparation. Nitrosyl d₁-heme complexes of WT and Y10F were obtained under anaerobic conditions in 50 mM bis-Tris buffer, pH 7.0. The enzyme was reduced with an excess (~200-fold) of sodium ascorbate, and after 1 h of incubation, ~50-fold of sodium nitrite was added to the enzyme. The final protein concentrations varied between 0.25 and 0.5 mM. In case of the dHis–NO complex preparation, a nitric oxide solution was added instead of the nitrite solution,^{26,27} keeping the same relative amount of ascorbate. Reduction and NO binding were monitored via UV–vis.²⁶ For a good glass formation upon freezing, glycerol was added (20–30% of the final volume). After the components were mixed, quartz capillaries were rapidly filled, and the solution was frozen by immersing the samples into liquid nitrogen.

For the deuterium exchange experiments, D₂O (D, 99.9%) and glycerol–(OD)₃ (D, 98%), both from Cambridge Isotope Laboratories, Inc., were used. All solutions were prepared under anaerobic conditions using a mixture of 50 mM bis-Tris (pH 7.0) in D₂O and 20–30% of glycerol. The stock solutions of sodium ascorbate and sodium nitrite were prepared, using the mixture of the buffer (D₂O) with deuterated glycerol, and degassed. The initial protein solution was diluted 10-fold

by the mixture of the deuterated buffer and glycerol, and then concentrated. Sodium ascorbate (~60 mM) was added to the concentrated D₂O exchanged protein and incubated for 1 h. Next, sodium nitrite/nitric oxide (for dHis–NO) (~15 mM) was added to give the final concentration of cd₁ NIR \approx 0.25–0.4 mM. The W-band EPR samples were prepared in a glovebox, where quartz capillaries were anaerobic filled with the NO-complex and immediately frozen in liquid nitrogen.

Spectroscopic Measurements. Pulse EPR and ENDOR measurements were carried out on a home-built W-band spectrometer operating at 94.9 GHz described elsewhere.²⁸ The main advantages of using high field are the enhancement of both the absolute sensitivity and the resolution. The increased sensitivity permits measurements of relatively small samples (2–3 μ L). The high resolution is essential for an accurate determination of the principal *g* values and it also allows one to perform orientation selective ENDOR experiments. Furthermore, the appreciably larger Zeeman interaction allows one to separate nuclei, which have close gyromagnetic ratios (γ), and to facilitate the detection of low γ nuclei such as ²H. In addition, the overlap of signals from strongly coupled ¹⁴N and weakly coupled ¹H, which is notorious at X-band, is not encountered at W-band.

Echo detected (ED) EPR spectra were recorded using the two-pulse echo sequence, $\pi/2-\tau-\pi-\tau$ -echo; the microwave (mw) pulse lengths were $t_{\pi/2} = 12.5$ ns and $t_{\pi} = 25$ ns, and the interpulse time τ was 350 ns. The magnetic field was calibrated using the ¹H Larmor frequency obtained from the ENDOR spectra. ENDOR spectroscopy is an alternative way to determine the NMR frequencies. It involves the application of both mw and radio frequency (RF) pulses. The standard experiments for measuring the ENDOR frequencies are the Mims²⁹ and Davies³⁰ sequences. The ENDOR spectrum is recorded by scanning the RF frequency, while monitoring the echo intensity of a stimulated (Mims) or a two-pulse echo (Davies). The ¹H ENDOR spectra were measured using the Davies ENDOR pulse sequence, $\pi-T-\pi/2-\tau-\pi-\tau$ -echo, with RF π pulse applied during the time interval *T*. Here, $t_{\pi/2} = 100$ ns, $t_{\pi} = 200$ ns, $\tau = 500$ ns, and $t_{RF} = 25$ μ s were used. The ²H ENDOR spectra were measured using the Mims ENDOR sequence $\pi/2-\tau-\pi/2-T-\pi/2-\tau$ -echo, with an RF pulse applied during the time interval *T*. The experimental conditions for Mims ENDOR were $t_{\pi/2} = 12.5$ ns, $\tau = 350$ ns (typical τ value that places the blind spots well outside the spectral range), and $t_{RF} = 45$ μ s. All ENDOR spectra were recorded using the random acquisition mode,³¹ with one shot for each point, and the total number of scans was 300–12000 depending on the S/N. The repetition time was 1 ms to which about 12 ms should be added that account for experimental parameters update and data transfer. All EPR measurements were carried out at 8 K.

Spectral simulations were performed to derive the spectroscopic parameters (*g* tensor, hyperfine tensor, nuclear quadrupole tensor, etc.). The echo detected (ED) EPR spectrum was simulated using Easy-Spin.^{32,33} The ¹H Davies and ²H Mims ENDOR were simulated using the Simbud³⁴ software, taking into account the effect of the blind spots.

Computational Details. Starting geometries for the cd₁ NIR active site model were created using the crystal structure of both the oxidized form (pdb 1nir¹⁵) and the reduced NO-bound form (pdb 1nno⁷). Although the resolution of 1nno is rather low (>2.65 Å), we considered this structure because of the changes observed in the organization of the amino acid residues in the distal side of the d₁-heme pocket, which may play an important role in the substrate attraction and release. The models comprise the d₁-heme, the NO group, the proximal histidine, and the side chain residues, His₃₂₇, His₃₆₉, and Tyr₁₀, each of which can form direct hydrogen bonds to the NO molecule. All side-chain residues were truncated at the α -carbon. For each of these starting structures, nine cluster models, varying in the protonation states of the two nitrogens of the two distal histidines His₃₂₇ and His₃₆₉, starting geometries were generated and optimized. The aim was to determine the

effect of the protonation states of these histidines on the structure and the EPR parameters.

Constraints were imposed on the initial structures to mimic the steric influence of the protein backbone. Because the protein backbone is not included in the cluster models, the side chains can drastically change their initial positions moving into free space, which is filled with protein chains in a real enzyme. To avoid such unrealistic rearrangements, side chains of interest were chosen and assigned to fragments. The fragments can then be connected with each other. The positions of all atoms within the fragments are fully optimized by the program, while the shortest distance between connected fragments, bond angles, and dihedrals angles, which contain this distance, were frozen (as in the crystal structure) to keep the fragments together and retain their orientation. Such calculations are referred to as “frozen”. This preliminary set of calculations using the 1nir as the initial structure showed that His₃₂₇ does not form H-bonds with the NO and practically does not affect the EPR parameters (Figures S1 and S2, Supporting Information). Therefore, we further concentrated on three representative structures A, B, and C with different protonation states of His₃₆₉ (Tables S1–S3, Supporting Information). We also carried out calculations on these three initial models with more relaxed constraints, where only the side-chains α -carbon were frozen, to ensure that a large enough range of structures are tested. These are referred to as relaxed structures. In addition, nine models were constructed starting from the 1nno crystal structure. In these structure optimizations we fixed only the position of the α -carbons.

The calculations were performed with the ORCA electronic structure package version 2.7³⁵ using various levels of DFT.³⁶ The models of the enzyme active site were optimized applying the BP86 functional³⁷ together with the resolution-of-the-identity (RI) approximation procedure within the Split-RI-J variant³⁸ for the Coulomb term.³⁹ The geometry optimizations were carried out using the triple- ζ quality TZVP basis set⁴⁰ applied for all atoms. An auxiliary basis set TZV/J⁴¹ was employed for the RI approximation.

For calculation of the EPR parameters, a flexible basis set was used for iron (CP(PPP)³⁵), nitrogen and oxygen atoms were treated with EPR-II basis set,⁴² carbons and hydrogens with SV(P).⁴³ To get reliable results from DFT calculations, the size of the integration grid was increased for the iron atom.⁴⁴ Fermi contact terms and spin-dipole contributions to the hyperfine coupling tensor were calculated as expectation values over the B3LYP ground-state spin density in the preliminary set of calculations of the nine frozen structures of the oxidized form (1nir) (Figure S1, Supporting Information). For the A, B, and C frozen (Figure S1, Supporting Information) and relaxed structures (Figure S7, Supporting Information) of 1nir and relaxed structures of the reduced NO-bound form (1nno) (Figure S10, Supporting Information), PBE has been used.^{45,46} The PBE functional was chosen because it has shown the best agreement with the experiment in the recent extensive investigation of Mb–NO.²² Second-order contributions to the hyperfine couplings that arise from spin–orbit coupling (SOC) as well as *g*-tensors were obtained using coupled perturbed Kohn–Sham theory.^{47,48} The spin–orbit coupling (SOC) operator was treated by spin–orbit mean-field (SOMF) approximation to the Breit–Pauli operator.⁴⁹

Nuclear quadrupole coupling constants, e^2qQ/h , were calculated from the electric field gradients V_{ii} according to the equation $e^2qQ/h = \text{const} \cdot V_{ii} \cdot Q$, where *Q* is the nuclear quadrupole moment ($Q(^{14}\text{N}) = 0.019$ barn).⁵⁰ The factor const = 234.96 converts e^2qQ/h from atomic to MHz units. The deviation of the nuclear quadrupole tensor from axial symmetry is given by the asymmetry parameter $\eta = (V_{xx} - V_{yy})/V_{zz}$ in a coordinate system where $|V_{zz}| > |V_{yy}| > |V_{xx}|$.

To consider the long-range electrostatic effects, self-consistent reaction field (SCRF) computations for each model were conducted using the COSMO model.⁵¹ The dielectric constant of chloroform (4.9) was used in the calculation, which is roughly representative of typical values

used for protein environments.⁵² All other COSMO parameters were default values. Moreover, to assess explicitly the hyperfine couplings for solvent's protons, each model was supplemented with three water molecules, whose positions were fully optimized. The hyperfine couplings of solvent's protons were then calculated under the same level of theory.

For the purpose of analysis, the unrestricted Kohn–Sham orbitals were transformed into the quasi-restricted orbitals⁵³ (QROs), which were then localized according to the Pipek–Mezey localization procedure.⁵⁴ Orbitals, densities, and structures were visualized with the Chimera program.⁵⁵

EXPERIMENTAL RESULTS

Echo-Detected EPR. The nitrosyl–heme complexes of the cd₁ NIR enzymes studied in this work were prepared under conditions where only the d₁-heme–NO complex is formed.²⁷ The echo-detected (ED) EPR spectrum of a frozen solution of d₁-heme–NO complex of WT cd₁ NIR of *P. aeruginosa* (WT–NO) at pH 7.0 and its simulation are shown in Figure 1a. The simulation of the spectrum revealed the presence of two paramagnetic species; a major species (~90%) with a rhombic g-factor [g_{\min} , g_{mid} , g_{\max}] = [1.960, 2.004, 2.062] and a minor contribution (~10%) of another rhombic conformation with [g_1 , g_2 , g_3] = [2.076, 2.025, 1.953]. The symmetry of the minor species is however ambiguous. We chose the symmetry which gives a best fit to the experimental data while noticing a possibility of the contribution of more than one minor species, that is, an axial and a rhombic one. A close look shows that the agreement between the simulated and the experimental spectra is not perfect at the high field edges of the spectrum, indicating the presence of a very small amount of a third species that we have ignored. The g-values of the major species are in good agreement with earlier reports in the literature where g_{mid} is referred to as g_{ZZ} , g_{\max} as g_{xx} and g_{\min} as g_{yy} .^{56–60} Different preparations, however, may differ in the relative amounts of the minor species, which nonetheless is always low. In our earlier report,⁶¹ the nitrosyl complexes were prepared in a phosphate buffer at pH 8.0, and the spectra have shown a lower amount of the minor species for both WT–NO and the nitrosyl complex of the Y10F mutant (Y10F–NO) as compared to the preparation in this work. The spectra of Y10F–NO and dHis mutants (dHis–NO) were similar to that of the WT–NO, as compared in Figure 1b, and may contain different amounts of the minor species (particularly dHis–NO). The simulation of the Y10F–NO spectrum, shown in Figure 1c, gave a major rhombic species (~85%) with [g_{\min} , g_{mid} , g_{\max}] = [1.970, 2.003, 2.062] noting a small difference in g_{\min} . Similar to WT–NO, a minor species with rhombic g, [g_1 , g_2 , g_3] = [2.090, 2.029, 1.955] was observed.

¹H Davies and ²H Mims ENDOR. To identify the protons forming hydrogen bonds with the NO group and to determine their hyperfine and quadrupole (for ²H nuclei) couplings, we have performed a set of orientation selective ¹H Davies and ²H Mims measurements at seven magnetic field positions within the EPR spectrum. The chosen field positions correspond to the principal g-values of the rhombic species and to some points in between. Because the rhombic species comprises 90% of the sample, in the following we have neglected any possible contributions of the minor species to the ENDOR spectra. The signals of H-bonded protons are identified by comparing the ¹H ENDOR spectra of samples prepared in H₂O with the ²H signals of a sample prepared in D₂O as shown in Figure 2. The scale of the ²H spectra was multiplied by $\gamma(^1\text{H})/\gamma(^2\text{H}) = 6.5$ for easy

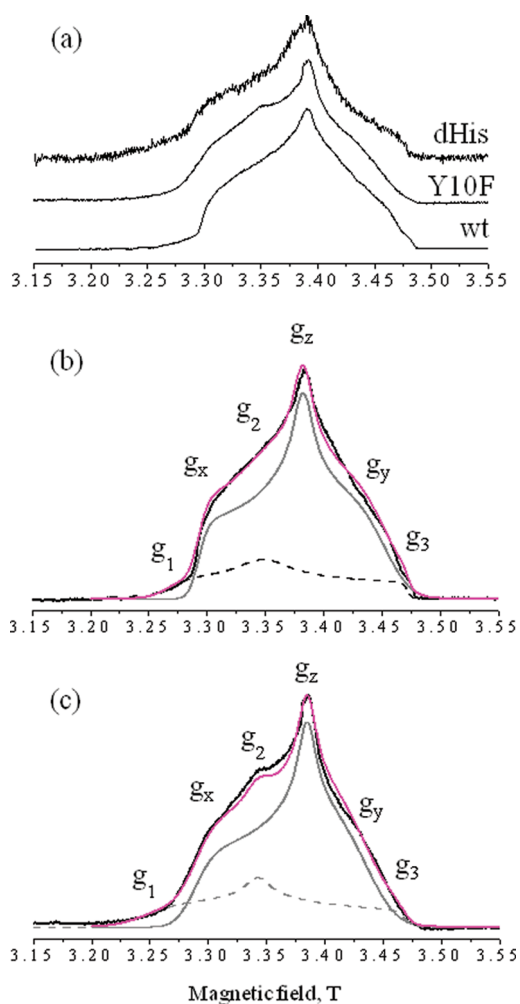


Figure 1. (a) Comparison of W-band ED EPR (8 K) spectra of WT–NO, Y10F–NO, and dHis–NO. Simulations (magenta) of the spectra of WT–NO (b) and Y10F–NO (c) as compared to the experimental spectra (black). The spectra of the major species (solid gray) and minor species (dashed gray) are shown as well. The simulation parameters are given in the text.

comparison with the ¹H spectra. This comparison clearly shows signals of exchangeable protons with a maximum hyperfine splitting of ~8 MHz appearing at $g = 2.002$ (marked with arrows). The difference in the outer edges of the spectra between the ¹H and ²H spectra is attributed to the ²H nuclear quadrupole interaction that effectively broadens the lines and occasionally quadrupolar splitting can be resolved. In principle, the differences could also arise from the blind spots in the Mims ENDOR spectra, but for the τ value of 0.350 μs used, the blind spots are well removed from the maximum splitting observed for ²H ($A < 1.5$ MHz). The largest detected splitting, ~8 MHz, is similar to that observed recently for the H-bond between the distal histidine and the nitrogen of the NO in Mb–NO.²² This suggests a similar H–N(O) distance, provided that the spin density distribution is similar.

A similar set of ENDOR measurements was carried out on Y10F–NO. In Figure 3, we compare ¹H Davies ENDOR spectra of WT–NO with those of Y10F–NO. We observe differences (marked by arrows) that are most significant at field positions corresponding to $g = 2.002$ and $g = 2.050$. The disappearance of

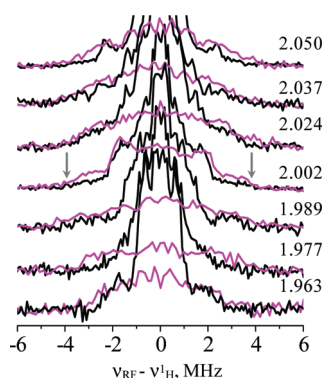


Figure 2. Comparison of orientation selective ^1H Davies ENDOR spectra of WT-NO in H_2O (black) with ^2H Mims ENDOR spectra of WT-NO in D_2O (magenta) at the indicated g values. The frequency scale of the ^2H spectra was multiplied by $\gamma(^1\text{H})/\gamma(^2\text{H}) = 6.5$. Arrows mark the large splitting of ~ 8 MHz.

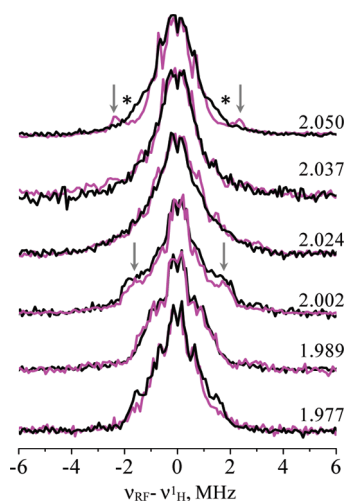


Figure 3. Comparison of orientation selective ^1H Davies ENDOR spectra of WT-NO (magenta) with that of Y10F-NO (black) at the indicated g values. Signals marked with arrows are tentatively assigned as H-bonded proton of Tyr₁₀, while those marked with asterisk are assigned as H-bonded proton of a histidine. Here, the spectra were normalized to the strongest signal.

the feature at ± 2.5 MHz (hyperfine coupling, $A = 5$ MHz, marked with arrows at $g = 2.050$) upon replacing Tyr₁₀ with Phe provides a tentative assignment of these signals to the OH proton of Tyr₁₀ that forms H-bond with the NO group. This comparison also reveals the appearance of new signals at ± 1.5 MHz in the Y10F-NO spectrum at $g = 2.050$ (marked with asterisk). These are tentatively assigned to the protons of one of the histidines, which were shifted due to the mutation. This assignment, however, does not agree with the crystal structure of WT-NO⁷ where Tyr₁₀ is situated at a distance too far to form an H-bond with the NO. An alternative assignment is that the 5 MHz doublet at the $g = 2.050$ spectrum of WT-NO is due to a histidine proton and the change in coupling represents the response of the histidine to the removal of the Tyr₁₀. These two alternatives were resolved using DFT calculations (see below).

To further highlight the differences between the WT-NO and the two mutants Y10F-NO and dHis-NO, we compared their ^2H Mims ENDOR spectra as well (see Figure 4). When

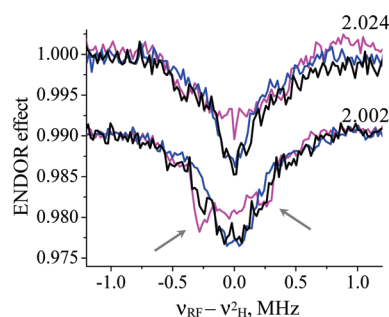


Figure 4. Comparison of the orientation selective ^2H Mims ENDOR spectra of WT-NO (magenta) with Y10F-NO (black) and dHis-NO (blue) at the indicated g values. Signals marked with arrows are assigned to H-bonded proton of Tyr₁₀ (first alternative). Here, the spectra are normalized according to the ENDOR effect, and the $g = 2.002$ spectra are shifted down by 0.01.

ENDOR spectra are compared, one has to pay a special attention to how the spectra were normalized, especially when the differences are associated with intensity changes, as opposed to line shifts. The simplest way is to normalize to the most intense signal, which often is the signal of distant protons at the nuclear Larmor frequency, particularly in Mims ENDOR. This approach is problematic, if there are changes in this region. Another way, the seemingly most proper one, is to present the spectra using the ENDOR effect (ε) given by:

$$\varepsilon = [I(RF_{\text{off}}) - I(RF_{\text{on}})] / I(RF_{\text{off}})$$

where $I(RF_{\text{on}})$ and $I(RF_{\text{off}})$ are the echo intensity with RF on and RF off resonance, respectively. Here, the problem is that ε depends on experimental conditions such as probe tuning and sample position and therefore requires special care in the adjustment of the experimental conditions. Therefore, only large changes that are consistent with other observations can be considered as reliable, unless some internal standard is used. The spectra in Figure 4 were normalized according to the ENDOR effect. The EPR signal intensity of dHis-NO was significantly lower than in the other two (see Figure 1b), and therefore we could not acquire a complete series of orientation selective ENDOR spectra for this sample. The comparison shown in Figure 4 suggests that the signals marked with arrows ($g = 2.002$) and corresponding to $A(^2\text{H}) = 0.5$ MHz (~ 3.3 MHz for ^1H) belong to the H-bonded OH proton of Tyr₁₀, according to the first assignment alternative, or one of the histidines, according to the second alternative. In Y10F-NO, the splitting of this doublet is somewhat smaller, and its intensity is weaker. It is assigned to an exchangeable proton of one of the histidines because it is absent in the spectrum of dHis-NO. The spectra of the mutants also show a significantly larger intensity at the Larmor frequency particularly at $g = 2.024$. This suggests that in the mutants there are more distant exchangeable protons, probably solvent molecules. The total width of the dHis spectrum is only slightly smaller than the other two, suggesting that there may be a water molecule in H-bond distance to the NO.

Through the ENDOR spectra of WT-NO and the mutants we identified two H-bonds to the NO group with substantial hyperfine coupling, but unlike Mb-NO,²² where the orientation selective ^2H spectra were well resolved and showed a clear line shape evolution that could be well reproduced by simulation, here the ^2H spectra do not show well-resolved distinct spectral

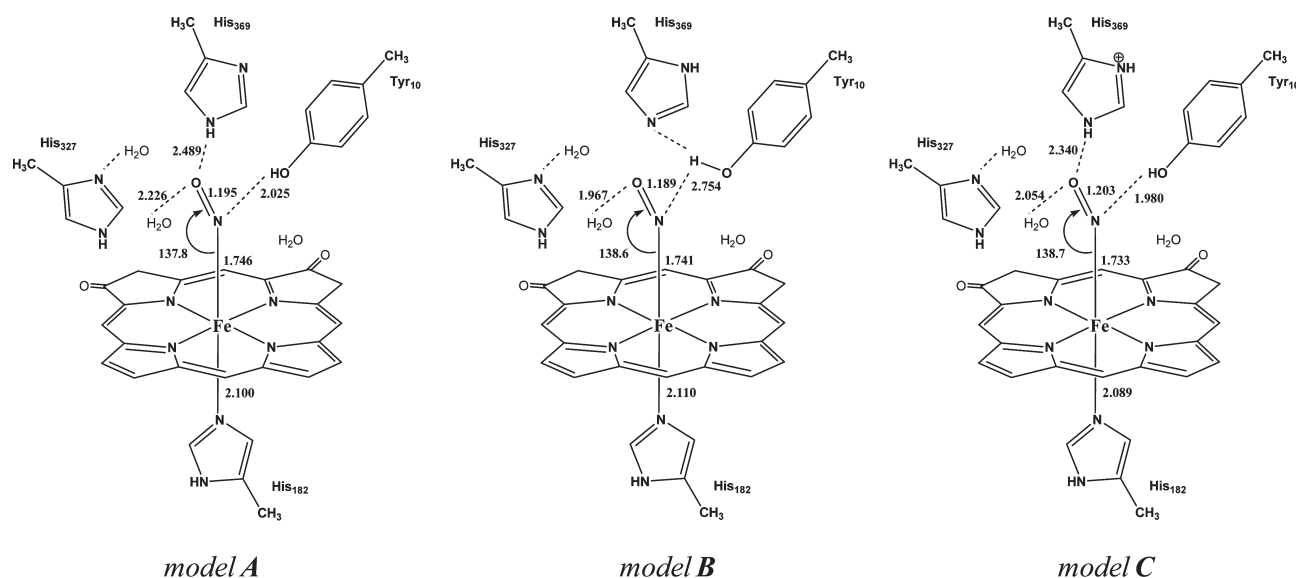


Figure 5. Calculated geometric parameters of the three selected frozen models (Å and deg).

features throughout the series due to the presence of the two H-bonds (or even more). Consequently, we did not attempt to simulate these spectra, which would require a large number of parameters (6 for each proton), but rather turned to DFT predictions to aid the spectral analysis. In our earlier study on Mb-NO,²² DFT calculations predicted well the experimental results and were found most helpful in spectral interpretation and assignment.

THEORETICAL RESULTS

Geometric Structure. In the DFT calculations, the initial structural models were based on two crystal structures, one of the oxidized cd₁ NIR from *P. aeruginosa* (pdb 1nir,¹⁵ resolution 2.15 Å), replacing the OH ligand with NO, and the second one is the reduced NO-bound form (pdb 1nno,⁷ resolution 2.65 Å). The major difference between the two structures that is relevant to this study is the location of Tyr₁₀, which is located away from the NO in 1nno, whereas in 1nir it is at a H-bond distance to the OH ligand of the d₁-heme. For each structure, nine models with different protonation states of the nitrogens of His₃₂₇ and His₃₆₉ were constructed (see Figure S1, Supporting Information), the geometries were optimized and EPR parameters were calculated. Some of the EPR parameters obtained with the B3LYP functional are summarized in Figure S2 (Supporting Information).

The preliminary calculations based on the 1nir structures showed that the protonation state of His₃₂₇ does not significantly influence the ¹⁴N hyperfine couplings of the NO and the coordinated nitrogen of the proximal His₁₈₂. Also, the ¹H hyperfine couplings of the OH of Tyr₁₀ and of His₃₆₉ are not affected by the protonation state of His₃₂₇ (Figure S2, Supporting Information). Furthermore, the ¹H and ¹⁴N nuclei of His₃₂₇ exhibit small hyperfine couplings. Therefore, we proceeded with the calculations focusing only on three models, hereafter referred to as models A, B, and C (they are shown in Figure 5 and correspond to models 1, 2, and 8 of the initial series of models) where three water molecules were added. The final set of calculations was done with the PBE functional because in our previous extensive study on Mb-NO we found that this is the most appropriate

choice for calculating the EPR parameters of Fe(II) nitrosyl systems.²² All calculated EPR parameters for these three models are given in Tables S1–S3, and some are compared in Figure S2, Supporting Information. We first present the results of the frozen structures (see Experimental Section).

In general, the predicted geometrical parameters (bond lengths, bond angles, and dihedral angles) are in good agreement with the X-ray derived geometry of the *P. aeruginosa* WT-NO complex (1nno)⁷ (see Table 1). A slight underestimation of the Fe–N(NO) (1.746 vs 1.803 Å) and an overestimation of the Fe–N(His₁₈₂) (2.100 vs 2.039 Å) distances were found. The Fe–N–O angle is also in good agreement with experiment (see Table 1). A major difference between the calculated and experimental structures concerns the distance of Tyr₁₀ from the NO. In the 1nno crystal structure, O_{Tyr10} is 4.9 Å away from the N(NO), whereas in our 1nir-based models, particularly A and C, O_{Tyr10} is closer to the NO. To make sure that this discrepancy is not an outcome of the fragment constraints applied, an additional set of calculations was carried out, where constraints were relaxed, and only the positions of the α-carbons of the amino acids were frozen in the geometry optimization. Also in this set the Tyr₁₀ remains close to the NO ligand. This is reflected in the calculated ¹H–O(Tyr₁₀) hyperfine coupling that will be discussed later. In the following, unless otherwise stated, models A, B, and C refer to the frozen structures.

In model B, His₃₆₉ is only protonated at N^δ, and this leads to conformational changes in the distal pocket (Figure 5). The hydroxyl group of Tyr₁₀ forms an H-bond with the N^ε of His₃₆₉; consequently, the distance between the Tyr₁₀ OH and the NO increases significantly. When the N^ε of His₃₆₉ is protonated, the OH of Tyr₁₀ is no longer H-bonded to His₃₆₉ and is available to form an H-bond with the nitrogen of the NO.

Electronic Structure and Bonding. The electronic structure of the low-spin {FeNO}⁷ complexes has been a subject of intensive theoretical and experimental studies.^{62,63} The three iron-based t_{2g} orbitals are doubly occupied. One of them has a non-bonding character and consists of the almost pure iron d_{xy} atomic orbital. The two remaining t_{2g} orbitals are dominated by the iron d_{xz} and d_{yz} and NO-π* contributions.

Table 1. Geometric Parameters (Å and deg) of Models A, B, and C^a

	Fe–N _{NO}	N–O _{NO}	Fe–N _{heme}	Fe–N _{His182}
model A	1.746	1.195	2.044–2.100	2.100
model B	1.741	1.189	2.010–2.076	2.110
model C	1.733	1.203	2.002–2.086	2.089
exp	1.803	1.153	2.052–2.085	2.039

	Fe–N–O	O _{NO} –H _{His369}	N _{NO} –H _{Tyr10}	O _{NO} –H _{Tyr10}	O _{NO} –H _{2O}
model A	137.8	2.489	2.025	2.555	2.269
model B	138.6		2.754	2.642	1.967
model C	138.7	2.340	1.980	2.524	2.054
exp	139.9	2.597 (to N _{His369})	5.0 (to O _{Tyr10})	4.2 (to O _{Tyr10})	3.310

^a The values in the “exp” line correspond to the crystal structure of WT–NO (1nno).⁷

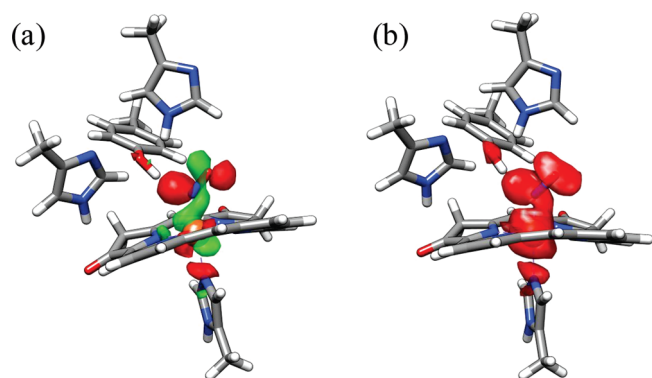


Figure 6. The SOMO orbital (a) and the spin density (b) of model A. (The water molecules are not shown.) Both the SOMO orbital and the spin density were calculated under the same level of theory as the EPR parameters.

The unpaired electron (see Figure 6) is situated in a strongly Fe–NO antibonding orbital with iron-3d and NO- π^* character. The composition of this orbital dominates the spin density contribution (and hence the EPR parameters) and, as discussed at length previously, is particularly sensitive to the theoretical method used. In this specific case, pure functional, such as PBE, is preferred over hybrid functionals.⁶⁴ According to the PBE results, the SOMO consists of mostly d_{z^2}/d_{xz} iron contributions (65%) with a major admixture of the NO- π^* -based orbital (33%) (Figure 6), similar to what was found for the Mb–NO complex.²²

Lehnert and co-workers^{65,66} have recently proposed that in six coordinated low-spin {FeNO}⁷ complexes the unpaired electron is mostly localized on the NO ligand (80%). The large spin population on the NO ligand was explained as a consequence of the sixth ligand coordination. Our d_1 -heme–NO structures are similar to the model systems discussed by Lehnert and co-workers,⁶⁶ and therefore the differences in spin populations may be caused by the applied density functional together with steric, electronic, and hydrogen-bonding effects. Taken together, this gives a complicated picture, which is reflected in bonding energies and finally also in observed g -values and hyperfine couplings.

The binding energies of the NO group were studied theoretically by different groups,^{64,67,68} and the results show that pure GGA functionals tend to overestimate the binding energy while hybrid functionals underestimate it. The value of 15 kcal/mol calculated here with the PBE functional for model C is in good

Table 2. Binding Energies (kcal/mol) and Spin Population on Fe, N(NO), and O(NO)^a

model	binding energies	Mulliken analysis			Loewdin analysis		
		Fe	N(NO)	O(NO)	Fe	N(NO)	O(NO)
model A	13	0.654	0.192	0.137	0.617	0.204	0.144
model B	10	0.553	0.301	0.128	0.541	0.280	0.146
model C	15	0.658	0.197	0.124	0.624	0.206	0.132

^a Calculations were performed using the B3LYP functional for bonding energies, and the PBE functional for spin populations.

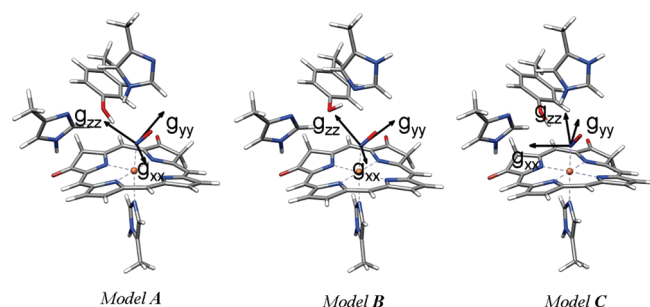
agreement with previous theoretical studies,⁶⁸ but still significantly smaller than the experimental value of 20 kcal/mol.⁶⁹ The calculated binding energy correlates with the number of the H-bonds in the system (see Table 2). Model B has only one H-bond with a water molecule and hence has the lowest binding energy, whereas model C has three hydrogen bonds with distances shorter than those of model A and consequently shows an increase in the binding energy. The physical origin of this effect is that H-bonds stabilize the NO- π^* based orbital, shifting it closer to the iron 3d-orbitals, and thus enhancing the back-bonding effect. Consistent with this notion, the shortest Fe–N(NO) distance is observed for the model C, confirming the strengthening of back-bonding for this complex. On the other hand, the spin population on the NO rises considerably for model B where the Tyr₁₀ does not form a hydrogen bond with the NO. This implies that hydrogen bonds to the O(NO) and N(NO) have a different influence on the electron and spin distribution in the complex as reported by Xu et al.⁷⁰ They have shown that H-bonding to O pulls electrons into the FeNO π^* orbital, thus strengthening the Fe–N bond while weakening the N–O bond. By contrast, H-bonding to N withdraws bonding electrons from both the Fe–N and the N–O bonds into a (partial sp^2) N-based nonbonding orbital. Hence, both bonds are weakened by this interaction. This effect is manifested in the lengthening of the Fe–N and the N–O bonds in model A relative to B.

■ CALCULATED EPR PARAMETERS

g -Tensor. The calculated g -values, listed in Table 3, are in reasonable agreement with the experimental values, except for g_{\max} (g_{xx}), which is too low for all three computational models. The underestimation of the g_{\max} is commonly found in DFT

Table 3. DFT Calculated g -Values of the Three Models As Compared To the Experimental Values

	exp	model A	model B	model C
$g_{\max} (g_{xx})$	2.062	2.030	2.030	2.030
$g_{\min} (g_{yy})$	1.960	1.983	1.969	1.984
$g_{\text{mid}} (g_{zz})$	2.004	2.005	2.000	2.007

**Figure 7.** Orientation of the g -tensor as obtained from DFT calculations on the frozen structures originating from 1nir. The water molecules are not shown.

g -tensor calculations on iron nitrosyl and is attributed to the limitations of the density functionals in predicting magnetic response properties. In particular, the excitation energies, calculated using DFT, enter implicitly in g values calculation and are usually not highly accurate and hence often cause errors in the computed g -tensors.^{71,72} Model B has lower g_{\min} and g_{mid} values, which may reflect the decrease of spin density on the Fe as a consequence of the removal of the H-bond of Tyr₁₀. The principal direction of the g -tensor is related to the NO geometry, with the orientation of g_{yy} (g_{\min}) approximately along the NO bond (13° , 9° , and 19° off for models A, B, and C, respectively), g_{zz} (g_{mid}) is perpendicular to it (in the plane of the Fe–NO unit), and g_{xx} (g_{\max}) is perpendicular to these two and 6° , 0° , and 3° off the heme plane for models A, B, and C, respectively, pointing toward the meso-carbon (see Figure 7). This orientation of the g -tensor is similar to that obtained in our earlier calculations on Mb–NO and has been confirmed experimentally.²²

¹⁴N Hyperfine Couplings of NO and Proximal His₁₈₂. The calculated ¹⁴N hyperfine and nuclear quadrupole parameters of the NO and of the coordinated ¹⁴N of the proximal His₁₈₂ of the three models are listed in Table 4. The most significant effect is the increase in the ¹⁴N(NO) hyperfine interaction when the Tyr₁₀ H-bond is removed, due to the shift of spin density onto the NO ligand. The values of models A and C are underestimated and are overall similar to those calculated for Mb–NO.²² In model B, they are overestimated. The principal axis system of the ¹⁴N(NO) hyperfine tensor is collinear with that of g . The calculated ¹⁴N(His₁₈₂) hyperfine coupling increases slightly upon removal of the H–N^ε(His₃₆₉) proton, which induces the removal of H-bond of Tyr₁₀ as well. Consequently, the spin population of ¹⁴N(His₁₈₂) increases slightly as reflected in the larger calculated hyperfine coupling of ¹⁴N(His₁₈₂).

The experimental values, listed in Table 4, were determined earlier by high field ENDOR and HYSCORE spectroscopy.⁶¹ The spectra of WT–NO and Y10F–NO were the same, suggesting that removal of Tyr₁₀ does not affect the spin density of ¹⁴N(His₁₈₂) and most probably also of the bonding properties of the Fe–N_{His} bond. The calculated principal hyperfine components of models A and C are underestimated as compared to

the experimental values, whereas those of B match the experimental values better, except for A_{yy} . The principal values were derived from earlier simulations. They were carried out under the assumption that the orientation of the ¹⁴N hyperfine and quadrupole interactions, which are related to the Fe–N_{His} direction, coincides with the orientation of g , where g_{zz} (g_{mid}) was assumed to be along the Fe–N(O) direction.⁶¹ Our recent Mb–NO²² and current DFT calculations showed that this is not the case and that g_{zz} (g_{mid}) is perpendicular to the NO direction (Figure 7). This wrong relative orientation of g and A tensors (due to wrong g orientation) led to an overestimated A_{yy} . Taking into account the correct orientation (which is similar in all models), we repeated the simulations of the HYSCORE and ENDOR spectra (the experimental and simulated HYSCORE spectra are shown in Figure S3, Supporting Information). The new values, (16.1, 16.3, 20.5) MHz, match those of model B in Table 4 and are close to the values obtained for Mb–NO, $A^{14}\text{N}(\text{His}_{93}) = (17.0, 17.3, 21.5)$ MHz.²² The difference only amounts to $\sim 6\%$, even though the heme structure and the residues in the distal side are quite different. To fit the experimental values, the hyperfine coupling values for model A would have to be increased by ~ 15 – 18% .

Hyperfine Couplings of the Tyr₁₀ and His₃₆₉ Protons. The calculated hyperfine and quadrupolar interactions of the H-bonded protons of Tyr₁₀ and His₃₆₉ for models A, B, and C are listed in Table 5. The larger spin density on the N(NO) as compared to the O(NO) (see Table 3) makes ENDOR more sensitive to H-bonds to the N(NO) because of their larger resolved ¹H hyperfine splitting. Remarkably, out of the three residues in the distal part of the heme pocket, only the H-bonded proton of Tyr₁₀ gives rise to large hyperfine couplings in all models. Simulations of the ¹H Davies and ²H Mims ENDOR spectra with the DFT parameters of models A and C (listed in Table 5) resulted in splittings that were significantly larger than those observed experimentally. When we reduced A_{xx} , A_{yy} , and A_{zz} of Tyr₁₀ OH of model A by a factor of 1.8 (see Table 5) without changing the orientation and the quadrupolar interaction parameters, a satisfactory fit was obtained for both the ¹H and the ²H ENDOR spectra, as shown in Figure 8a and b, respectively. Simulations using the parameters of model C, also with scaling of 1.8 for the hyperfine of Tyr₁₀, gave a reasonable fit (Figures S4 and S5, Supporting Information), although not as good as for model A. In model B, one of the water protons has an A_{zz} value close to 8 MHz, which is close to the experimentally observed A_{\max} . Simulations using the calculated hyperfine parameters of this proton did not reproduce the line shape evolution of the orientation selective spectra (Figures S4 and S5, Supporting Information).

In all models, except for one water molecule in model B, the calculated hyperfine couplings of the water molecules were relatively small (see Tables S1–S3), and therefore they were not included in the simulations. On the basis of the DFT calculations, we assign the large couplings observed in WT–NO to the H-bonded proton of Tyr₁₀. We hypothesized that the rather large scaling factor required to fit the DFT results to the experimental spectra might originate from problems with the crystal derived structure constraints on our model. To address this question, a rigid scan of the N(NO)–H(O–Tyr₁₀) distance was conducted while keeping the relative orientations fixed. The distance was increased in steps of 0.2 Å. The calculated principal components of the hyperfine tensor as well as the spin populations on the iron and NO fragments are shown in the Supporting Information, Figure S6. For a distance of 2.57 Å, the obtained

Table 4. DFT (PBE) Calculation of the Hyperfine (A) and Nuclear Quadrupole (e^2Qq/h) Coupling Constants (MHz) of ^{14}N of the NO and Proximal His₁₈₂ Ligand^a

	exp	model A	model B	model C
$^{14}\text{N}(\text{NO})^{61}$				
A_{xx} MHz	26.9	16.4 (14.6)	36.8 (34.8)	15.9 (15.3)
A_{yy} MHz	33.5	20.9 (19.3)	39.0 (37.1)	20.9 (20.2)
A_{zz} MHz	64.5	55.0 (53.5)	82.7 (81.1)	55.5 (55.1)
a_{iso} MHz	41.6	30.8 (29.2)	52.9 (51.0)	30.8 (30.2)
$(\alpha, \beta, \gamma)_A$		[90 119 11]	[109 93 2]	[86 59 343]
e^2qQ/h , MHz		−2.499 (−2.554)	−2.437 (−2.486)	−2.720 (−2.715)
η		0.848 (0.823)	0.921 (0.899)	0.733 (0.737)
$(\alpha, \beta, \gamma)_Q$		[89 119 97]	[110 94 92]	[83 58 252]
$^{14}\text{N}(\text{His}_{182})$				
A_{xx} MHz	16.0 ⁶¹ (16.0) ^b	13.1 (13.1)	16.1 (16.0)	11.5 (11.6)
A_{yy} MHz	19.5 ⁶¹ (16.3)	13.4 (13.3)	16.3 (16.3)	11.7 (11.8)
A_{zz} MHz	19.5 ⁶¹ (20.5)	17.2 (17.4)	20.4 (20.6)	15.4 (15.7)
a_{iso} MHz	18.3 ⁶¹ (17.6)	14.6 (14.6)	17.6 (17.7)	12.9 (13.1)
$(\alpha, \beta, \gamma)_A$		[213 87 4]	[49 90 352]	[31 93 86]
e^2qQ/h , MHz	2.6	−2.268 (−2.112)	−2.347 (−2.209)	−2.110 (−2.024)
η		0.597 (0.687)	0.555 (0.628)	0.701 (0.758)
$(\alpha, \beta, \gamma)_Q$		[140 95 87]	[54 90 266]	[35 87 355]

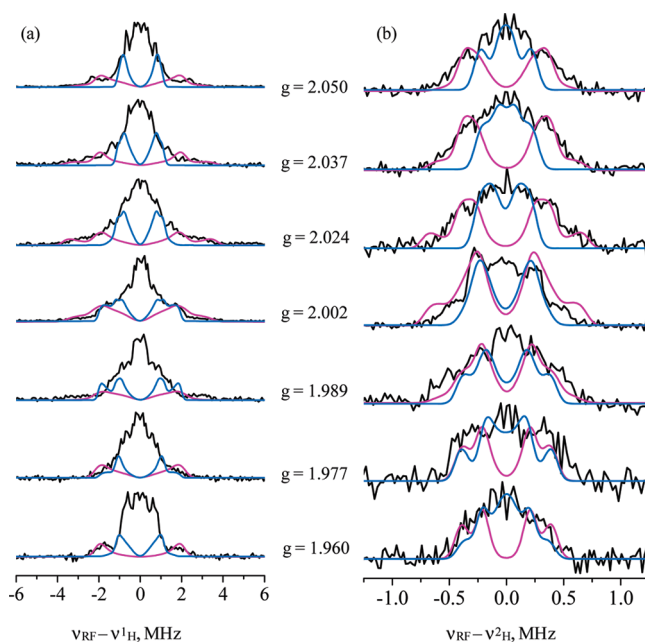
^aThe corresponding Euler angles (α, β, γ) (deg) relate the hyperfine and quadrupole tensor's orientation with g ($g_{\text{min}}, g_{\text{mid}}, g_{\text{max}}$). The values in parentheses were calculated with inclusion of COSMO. ^bThe values obtained after using the correct g -orientation in the simulations.

Table 5. DFT (PBE) Calculation of Hyperfine (A) and Nuclear Quadrupole (e^2Qq/h) Coupling Constants (MHz) of Protons of Tyr₁₀ and His₃₆₉, Which Are H-Bonded to the NO Group^a

	model A	model B	model C
$^1\text{H}/^2\text{H}(\text{Tyr}_{10})$			
A_{xx} MHz	−7.9 (−7.6)	−3.1 (−3.1)	−8.6 (−8.4)
A_{yy} MHz	−6.5 (−6.2)	−1.9 (−1.9)	−6.8 (−6.6)
A_{zz} MHz	13.6 (14.0)	4.3 (4.4)	14.6 (14.9)
a_{iso} MHz	−0.3 (0.1)	−0.2 (−0.2)	−0.3 (0.0)
$(\alpha, \beta, \gamma)_A$	[81 124 127]	[77 106 300]	[73 53 75]
e^2qQ/h , MHz	0.249 (0.248)	0.166 (0.166)	0.241 (0.241)
η	0.12 (0.119)	0.175 (0.175)	0.124 (0.124)
$(\alpha, \beta, \gamma)_Q$	[74 103 195]	[0 53 348]	[40 55 104]
$^1\text{H}/^2\text{H}(\text{His}_{369})$			
A_{xx} MHz	−2.4 (−2.4)		−2.7 (−2.7)
A_{yy} MHz	−1.6 (−1.6)		−1.6 (−1.6)
A_{zz} MHz	4.0 (4.0)		4.2 (4.2)
a_{iso} MHz	0.0 (0.0)		0.0 (0.0)
$(\alpha, \beta, \gamma)_A$	[58 95 296]		[42 71 50]
e^2qQ/h , MHz	0.26 (0.258)		0.219 (0.221)
η	0.088 (0.087)		0.082 (0.085)
$(\alpha, \beta, \gamma)_Q$	[21 85 107]		[202 76 345]

^aThe corresponding Euler angles (α, β, γ) (deg) relate the hyperfine and quadrupole tensor's orientation with respect to g ($g_{\text{min}}, g_{\text{mid}}, g_{\text{max}}$). The values in parentheses were calculated with COSMO.

hyperfine values, $A = (-3.5, -2.9, 8)$ MHz, are close to the experimental values ($A = (-4.2, -3.4, 7.7)$ MHz). This distance would amount to a change of ~ 0.5 Å in the N(NO)–H–(O–Tyr₁₀) distance. We do think that movements of this size

**Figure 8.** Experimental (black) and simulated (magenta/blue) ^1H Davies ENDOR spectra (a) and ^2H Mims ENDOR spectra (b) of WT–NO. The simulations of the H-bonded proton of Tyr₁₀ (magenta) and His₃₆₉ (blue) are shown individually. The parameters used for the simulation are given in Table 5 for model A except the hyperfine couplings of Tyr₁₀ that were scaled down by a factor of 1.8.

relative to the crystal structure may well take place and may help to explain the apparent discrepancy between theoretical and experimental values.

To summarize, of the three models A, B, and C, we do not find a single model that best fits all of the relevant experimental

parameters: the principal values of g the hyperfine interaction of $^{14}\text{N}(\text{NO})$ and $^{14}\text{N}(\text{His}_{182})$, and the $^1\text{H}/^2\text{H}$ ENDOR spectra. Model B provides better agreement with the $^{14}\text{N}(\text{His}_{182})$ data, while in model A these hyperfine values were off by 15–18%. In contrast, model A could reproduce the orientation selective $^1\text{H}/^2\text{H}$ ENDOR spectra reasonably well (better than model B) after invoking a single scaling factor for the hyperfine coupling of the exchangeable protons of Tyr_{10} . The necessity of this scaling factor may well have to do with problems with the crystal structure derived constraints. For model B, it would be difficult to account for the spectra of Y10F as His_{369} does not have a proton to contribute to the spectrum. Therefore, we chose model A as the preferred model.

We have also checked the agreement between the geometrically relaxed models A, B, and C originating from 1nir structure and optimized without constraints (see Figure S7) and the experimental data (see Tables S4–S7 and Figures S8, S9). The behavior, in general, is similar to the frozen models (see Figures 8, S4, and S5), and the $^1\text{H}-\text{O}(\text{Tyr}_{10})$ in models A and C is close to the NO. While the $^{14}\text{N}(\text{His}_{182})$ hyperfine values remained almost unchanged, the agreement of the calculated orientation selective $^1\text{H}/^2\text{H}$ ENDOR spectra with the experimental ones was inferior to the frozen structures because of changes in ligand orientation that would be prevented by the protein backbone in the real system.

Unlike the structures that originated from the oxidized enzyme, where His_{327} did not show any significant H-bonding to the NO, in the relaxed structures that originated for the reduced NO-bound structure (pdb 1nno) all three residues, His_{327} , His_{369} , and Tyr_{10} , depending on the histidines' protonation states, formed H-bonds with the NO (Figure S10). The EPR parameters (see Tables S8–S11) obtained from the nine structures gave in general similar agreement to that observed in models A–C for the ^{14}N hyperfine couplings of NO and His_{182} (these are summarized in Figure S11). Here too, protonation of N^ϵ of His_{369} permits forming of an H-bond between the $^1\text{H}-\text{O}(\text{Tyr}_{10})$ and NO. Out of the nine models, we selected those that gave the largest ^1H hyperfine coupling, models 5 and 9, and calculated the orientation selective $^1\text{H}/^2\text{H}$ ENDOR spectra of all three residues, His_{327} , His_{369} , and Tyr_{10} . These are compared to the experimental spectra in Figures S12 and S13. The agreement for model 5 is not satisfactory. Model 9 is rather similar to model A in terms of the positions of distal residues with respect to the NO. In this model, all nitrogens of His_{369} and His_{327} are protonated, and His_{369} and Tyr_{10} form H-bonds with the NO, both generating comparable significant hyperfine couplings. The main difference relative to model A is the longer distance of the $^1\text{H}-\text{O}(\text{Tyr}_{10})$ to the $\text{N}(\text{NO})$ and a closer distance to the $\text{O}(\text{NO})$ in model 9. Here, the magnitude of the hyperfine couplings is close to the experimental values, but the line shape evolution of the orientation selective spectra is not well reproduced and is inferior to model A. Interestingly, in this model, the $^{14}\text{N}(\text{His}_{182})$ hyperfine couplings are also underestimated as compared to the experiment (by $\sim 10\%$).

DISCUSSION

In this work, we focused on the identification and characterization of the H-bonds formed by amino acid residues in the distal pocket of the reduced d_1 -heme with the NO ligand in WT–NO and two mutants, Y10F–NO and dHis–NO, in

frozen solutions. The protonation state of the histidines is unknown because the resolution of the X-ray determined structure of WT–NO is too low to allocate the position of the protons. We have used W-band ENDOR to detect the H-bonds and carried out detailed DFT calculations on structures with various possible protonation states of the distal histidines to interpret the experimental results and related them to structure. These revealed a correlation between the histidines' protonation states: the position of the residues and the H-bonds to the NO. The calculations also highlighted expected conformational changes upon variations in the H-bond network that were in line with the experimental observations found in the mutants. The DFT calculations showed that for the structure that agrees best with the experimental results (model A), the conserved His_{327} residue has no H-bonds to the NO. It was, however, previously shown to play an important role in catalysis.^{10,16} A possible explanation of this finding can be that His_{327} maintains a positive charge in the active site, which in turn helps to guide negatively charged substrates like nitrite to the active center. In WT–NO (pH = 7.0), we identified two H-bonds to the NO group; one is from the OH of Tyr_{10} , and the other is from the protonated N^ϵ of His_{369} . This is in contrast to the crystal structure of WT–NO, which shows that upon reduction and NO binding the Tyr_{10} is removed from the close vicinity of the iron and is too far to form an H-bond with the NO.⁷

The experimental results on WT–NO and its mutants, together with the DFT calculations, indicate that the H-bond network is dynamic. Comparison of the ^1H Davies ENDOR spectra of WT–NO and Y10F–NO clearly reveals a disappearance of signals and appearance of new ones (see Figure 3). Because in Y10F Tyr is removed, we assigned the disappearing signals in WT–NO to the $\text{H}(\text{OH})$ of Tyr_{10} and the new signals in the Y10F–NO ENDOR spectra to an H-bond of the exchangeable proton of His_{369} . From the analysis of the ENDOR spectra and the DFT results, we suggest a cooperative behavior for Tyr_{10} and His_{369} . The H-bond formed between the protonated N^ϵ of His_{369} to $\text{O}(\text{NO})$ allows positioning Tyr_{10} next to the NO. Upon mutation of the Tyr_{10} to Phe, His_{369} becomes closer to the NO, yielding a larger ^1H hyperfine splitting for the H-bonded proton. Unlike Y10F–NO, a distinct substantial hyperfine coupling corresponding to a proton H-bonded to the NO has not been observed for the dHis mutant. This suggests that in this mutant, the Tyr_{10} is displaced such that it cannot form an H-bond with the $\text{N}(\text{NO})$. The total width of the spectrum, however, suggests that there may be a water molecule (or more) coordinated to the NO ligand.

Figure 9 summarizes the dynamic H-bonding network and conformational changes caused by mutations based on the EPR experimental data and the DFT calculations. It is clear that a change in one of the residues within the d_1 -heme active site does affect the strength and position of the H-bonds formed by the other residues. In fact, in Y10F–NO, His_{369} moves closer to the NO, and its hydrogen bond becomes shorter, whereas mutation of both distal histidines displaces Tyr_{10} removing its H-bond. Accordingly, one may speculate that any event that changes the location or protonation state of one residue is likely to affect the whole active site structure. Moreover, the DFT calculations of the bonding energies, charge, and spin distributions suggest that the hydrogen-bond network of the active site may play some role in the product release. As discussed at length previously, the low-spin $\{\text{FeNO}\}^7$ complexes are known to be very stable, and thus the NO release should be very slow if it occurs from the

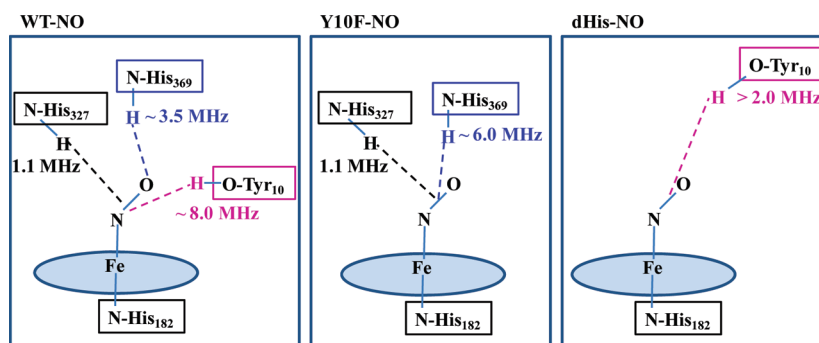


Figure 9. Proposed conformational changes in the distal pocket of the d_1 -NO complex caused by mutation. The dashed lines correspond to the H-bonds. When it is not known whether the bond is with O(NO) or N(NO), we mark it midway.

Fe(II) state. Nevertheless, a recent kinetic investigation of Rinaldo et al.¹⁰ has shown that NO dissociates from the reduced d_1 -heme considerably faster than from other hemes.

The electronic effects that are responsible for the stability of the ferrous–nitroso complexes are the back bonding between the ferrous iron and the NO adduct, the number and strength of the H-bonds in the active site, and the spatial conformation of the NO on the porphyrine plane. The latter is naturally affected by the structure of the heme itself. Here, we consider the contribution of two first effects that are strongly influenced by H-bonding to protein residues, thereby focusing on the effects of the protein and not on the contribution of unique d_1 heme, which is probably very significant. In the initial step of the reduction process, the substrate attraction and activation stage, the active site histidines are assumed to be protonated to create a positive electrostatic potential responsible for the negatively charged NO_2^- attraction. After the substrate binding, reduction proceeds through cleavage of one of the N–O bonds and the formation of a water molecule, converting ferrous–nitrite complex to the $\{\text{FeNO}\}^6$ adduct (iron is in ferric state). The source of protons for the formed water molecule is most probably His₃₆₉ and His₃₂₇. At this stage, the NO can be released from the Fe(III) state not forming the stable $\{\text{FeNO}\}$.⁷ However, in the case that there is an electron transfer from the reduced c heme to the d_1 heme before the NO release, the stable $\text{Fe}\{\text{NO}\}^7$ complex forms. Therefore, if N^ϵ -His₃₆₉ remains deprotonated and Tyr₁₀ is not H-bonded (model B), NO release may be facilitated by the small number of H-bonds. Alternatively, if the N^ϵ His₃₆₉ does reprotonate fast (models A and C that fit the experimental results) and forms an H-bond to the O(NO), which stabilize the Fe(II)–NO bond, this stabilization is counteracted by the H-bond of the Tyr₁₀ with the N(NO). The latter populates the (partial sp^2) N-based nonbonding orbital, thus weakening the Fe–N(NO) bond, and this in turn should facilitate NO release.

To summarize, we point out that a highly mobile and flexible H-bonding network at the active site is needed for accomplishing the effective reduction process. The positively charged histidines attract the substrate, donate protons, thereby cleaving one N–O bond in NO_2^- , and work in concert with Tyr₁₀, which, in the case of a quick reduction of the metal prior to NO release, forms H-bond to N(NO), lowering the amount of back-donation from the Fe(II). Hence, we suggest that the role of Tyr₁₀ can be considered as a measure against the formation of a too stable $\text{Fe}\{\text{NO}\}^7$ product by facilitating NO release. However, because Y10F was reported to be active,¹⁷ this route

is considered as the less favorable one and NO release probably does occur primarily through the $\text{Fe}\{\text{NO}\}^6$ state. Alternatively, in the absence of Tyr₁₀, the role of its H-bond may be played by His₃₂₇, as we see a rearrangement in the H-bonding upon the Y10F mutation. To corroborate the suggested role of Tyr₁₀, the NO release rates from Y10F–NO and WT from *Pseudomonas stutzeri*, which does not have an equivalent of Tyr₁₀, should be measured.

Another interesting observation of this work is the rather insensitivity of the hyperfine coupling of the ^{14}N of the axial ligand and the NO to variation in the H-bond network to the NO at the distal pocket. Even more surprising is the similarity to Mb–NO (within $\sim 6\%$), which has a different heme altogether and only one H-bond to the NO. Finally, both Y10F–NO and dHis–NO were found to exhibit weak interactions with distant water molecules, suggesting some opening of the pocket as compared to the WT. This observation implies that the conformational changes observed in the crystal structure of the single mutants (H327A and H369A), involving the c-heme domain relocation and opening of the distal pocket, are likely to take place also in solution. On the other hand, in the WT enzyme, all available data suggest that the active site is more “closed” to solvent.

CONCLUSIONS

In this work, we have once more demonstrated the value of high field ENDOR combined with DFT calculations for the characterization of H-bonds and highlighted the important role of DFT in assigning and interpreting ENDOR spectra in terms of structural details for complicated systems. We have shown that the NO in the nitrosyl d_1 -heme complex of cd_1 NIR forms H-bonds with Tyr₁₀ and His₃₆₉ that affect the stabilization of the NO complex. The second conserved His₃₂₇ appears to be less involved in NO stabilization by H-bonding. This is in contrast to the WT–NO crystal structure where Tyr₁₀ is not at an H-bond distance from the NO. We have also observed a larger solvent accessibility to the distal pocket in the mutants as compared to the WT. Finally, it is clear from this work that the H-bonding network within the active site is dynamic and that a change in one of the residues does affect the strength and position of the H-bonds formed by the other ones. In the Y10F mutant, His₃₆₉ moves closer to the NO, and its hydrogen bond is shorter, whereas mutation of both distal histidines displaces Tyr₁₀, removing its H-bond.

■ ASSOCIATED CONTENT

S Supporting Information. Structures and tables with the DFT calculated EPR parameters of the various protonation states of the nitrosyl d₁-heme active sites, figures comparing experimental and calculated ¹H/²H ENDOR spectra and simulations of the W-band HYSCORE spectra of WT–NO. This material is available free of charge via the Internet at <http://pubs.acs.org>.

■ AUTHOR INFORMATION

Corresponding Author

daniella.goldfarb@weizmann.ac.il; neese@thch.uni-bonn.de

■ ACKNOWLEDGMENT

This research was supported by the German-Israel Foundation for Scientific Research (D.G. and F.N.). D.G. holds the Erich Klieger Chair of Chemical Physics. Funds from the Ministero della Università di Italy [RBRN07BMCT, RBRN04PWNC] and from the University of Rome La Sapienza to F.C. are gratefully acknowledged.

■ REFERENCES

- (1) Yamanaka, T.; Okunuki, K. *Biochim. Biophys. Acta* **1963**, *67*, 394–406.
- (2) Horio, T.; Higashi, T.; Sasagawa, M.; Kusai, K.; Nakai, M.; Okunuki, K. *Biochem. J.* **1960**, *77*, 194–201.
- (3) Zumft, W. G. *Mol. Biol. Rev.* **1997**, *61*, 533–616.
- (4) Allen, J. W. A.; Watmough, N. J.; Ferguson, S. J. *Nature* **2000**, *7*, 885–888.
- (5) Rinaldo, S.; Cutruzzolà, F. *Nitrite Reductases in Denitrification in Biology of the Nitrogen Cycle*; Elsevier: Amsterdam, 2007.
- (6) Vijgenboom, E.; Busch, J. E.; Canters, G. W. *Microbiology* **1997**, *143*, 2853–2863.
- (7) Nurizzo, D.; Cutruzzolà, F.; Areses, M.; Bourgeois, D.; Brunori, M.; Cambillau, C.; Tegoni, M. *Biochemistry* **1998**, *37*, 13987–13996.
- (8) Silvestrini, M. C. *Biol. Chem.* **1990**, *265*, 11783–11787.
- (9) Averill, B. A. *Chem. Rev.* **1996**, *96*, 2951–2964.
- (10) Rinaldo, S.; Arcovito, A.; Brunori, M.; Cutruzzolà, F. *J. Biol. Chem.* **2007**, *282*, 14761–14767.
- (11) Moore, E. G.; Gibson, Q. H. *J. Biol. Chem.* **1976**, *251*, 2788–2794.
- (12) Sarti, P.; Giuffrè, A.; Forte, E.; Mastronicola, D.; Barone, M. C.; Brunori, M. *Biochem. Biophys. Res. Commun.* **2000**, *274*, 83–187.
- (13) Borisov, V. B.; Forte, E.; Sarti, P.; Brunori, M.; Konstantinov, A. A.; Giuffrè, A. *Biochem. Biophys. Res. Commun.* **2007**, *355*, 97–102.
- (14) Rinaldo, S.; Brunori, M.; Cutruzzolà, F. *Plant Signaling Behav.* **2008**, *3*, 135–136.
- (15) Nurizzo, D.; Silvestrini, M. C.; Mathieu, M.; Cutruzzolà, F.; Bourgeois, D.; Fülöp, V.; Hajdu, J.; Brunori, M.; Tegoni, M.; Cambillau, C. *Structure* **1997**, *5*, 1157–1171.
- (16) Cutruzzolà, F.; Brown, K.; Wilson, E. K.; Bellelli, A.; Arese, M.; Tegoni, M.; Cambillau, C.; Brunori, M. *Proc. Natl. Acad. Sci. U.S.A.* **2001**, *98*, 2232–2237.
- (17) Cutruzzolà, F.; Arese, M.; Grasso, S.; Bellelli, A.; Brunori, M. *FEBS Lett.* **1997**, *412*, 365–369.
- (18) Brown, K.; Roig-Zamboni, V.; Cutruzzolà, F.; Arese, M.; Sun, W.; Brunori, M.; Cambillau, C.; Tegoni, M. *J. Mol. Biol.* **2001**, *312*, 541–554.
- (19) Kababya, S.; Nelson, J.; Carlos, C.; Neese, F.; Goldfarb, D. *J. Am. Chem. Soc.* **2006**, *128*, 2017–2029.
- (20) Baute, D.; Arieli, D.; Neese, F.; Zimmerman, H.; Weckhuysen, B. M.; Goldfarb, D. *J. Am. Chem. Soc.* **2004**, *126*, 11733–11745.
- (21) Carmieli, R.; Larsen, T. M.; Reed, G. H.; Zein, S.; Neese, F.; Goldfarb, D. *J. Am. Chem. Soc.* **2007**, *129*, 4240–4252.
- (22) Radoul, M.; Sundararajan, M.; Potapov, A.; Riplinger, C.; Neese, F.; Goldfarb, D. *Phys. Chem. Chem. Phys.* **2010**, *12*, 7276–7289.
- (23) Parr, S.; Barber, D.; Greenwood, C.; Brunori, M. *Biochem. J.* **1977**, *167*, 447–455.
- (24) Wilson, E. K.; Bellelli, A.; Liberti, S.; Arese, M.; Grasso, S.; Cutruzzolà, F.; Brunori, M.; Brzezinski, P. *Biochemistry* **1999**, *38*, 7556–7564.
- (25) Silvestrini, M. C.; Cutruzzolà, F.; D'Alessandro, R.; Brunori, M.; Fochesato, N.; Zennaro, E. *Biochem. J.* **1992**, *285*, 661–666.
- (26) Silverstrini, M. C.; Colosimo, A.; Brunori, M.; Walsh, T. A.; Barber, D.; Greenwood, C. *Biochem. J.* **1979**, *183*, 701–709.
- (27) Nurizzo, D.; Cutruzzolà, F.; Arese, M.; Bourgeois, D.; Brunori, M.; Cambillau, C.; Tegoni, M. *J. Biol. Chem.* **1999**, *274*, 14997–15004.
- (28) Goldfarb, D.; Lipkin, Y.; Potapov, A.; Gorodetsky, Y.; Epel, B.; Raitsimring, A. M.; Radoul, M.; Kaminker, I. *J. Magn. Reson.* **2008**, *194*, 8–15.
- (29) Mims, W. B. *Proc. R. Soc. London* **1965**, *283*, 452–457.
- (30) Davies, E. R. *Phys. Lett. A* **1974**, *47*, 1–2.
- (31) Epel, B.; Arieli, D.; Baute, D.; Goldfarb, D. *J. Magn. Reson.* **2003**, *164*, 78–83.
- (32) Stoll, S.; Schweiger, A. *J. Magn. Reson.* **2006**, *178*, 42–55.
- (33) http://www.boep.specman4ep.com/kv_intro.html.
- (34) <http://chem.arizona.edu/rss/epr/software.html>.
- (35) Neese, F. *ORCA – an ab initio, Density Functional and Semiempirical Program Package 2.7*; University Bonn: Germany, 2009.
- (36) Neese, F. *J. Biol. Inorg. Chem.* **2006**, *11*, 702–711.
- (37) (a) Perdew, J. P. *Phys. Rev. B* **1986**, *33*, 8822–8824. (b) Becke, A. D. *J. Chem. Phys.* **1986**, *84*, 4524–4529.
- (38) Neese, F. *J. Comput. Chem.* **2003**, *24*, 1740–1747.
- (39) (a) Baerends, E. J.; Ellis, D. E.; Ros, P. *Chem. Phys.* **1973**, *2*, 41–51. (b) Dunlap, B.; Connolly, J. W. D.; Sabin, J. R. *J. Chem. Phys.* **1979**, *71*, 3396–3402.
- (40) Schaefer, A.; Huber, C.; Ahlrichs, R. *J. Chem. Phys.* **1994**, *100*, 5829–5835.
- (41) (a) Eichkorn, K.; Treutler, O.; Öhm, H.; Häser, M.; Ahlrichs, R. *Chem. Phys. Lett.* **1995**, *240*, 283–290. (b) Eichkorn, K.; Weigend, F.; Treutler, O.; Ahlrichs, R. *Theor. Chem. Acc.* **1997**, *97*, 119–124.
- (42) Barone, V. In *Recent Advances in Density Functional Methods*; Chong, D. P., Ed.; World Scientific Publ. Co.: Singapore, 1996.
- (43) Schaefer, A.; Horn, H.; Ahlrichs, R. *J. Chem. Phys.* **1992**, *97*, 2571–2577.
- (44) Neese, F. *Inorg. Chim. Acta* **2002**, *337C*, 181–192.
- (45) Perdew, J. P.; Burke, K.; Ernzerhof, M. *Phys. Rev. Lett.* **1996**, *77*, 3865–3868.
- (46) Perdew, J. P.; Burke, K.; Ernzerhof, M. *Phys. Rev. Lett.* **1996**, *77*, 3865; **1997**, *78*, 1396.
- (47) Neese, F. *J. Chem. Phys.* **2001**, *115*, 11080–11096.
- (48) Neese, F. *J. Chem. Phys.* **2003**, *118*, 3939–3948.
- (49) Neese, F. *J. Chem. Phys.* **2005**, *122*, 34107.
- (50) Tokman, M.; Sundholm, D.; Pykkö, P.; Olsen, J. *J. Chem. Phys. Lett.* **1997**, *265*, 60–64.
- (51) Sinnecker, S.; Rajendran, A.; Klamt, A.; Diedenhofen, M.; Neese, F. *J. Phys. Chem. A* **2006**, *110*, 2235–2245.
- (52) Siegbahn, P. E. M.; Blomberg, M. R. A. *Chem. Rev.* **2000**, *100*, 421–437.
- (53) Neese, F. *J. Am. Chem. Soc.* **2006**, *128*, 10213–10222.
- (54) Pipek, J.; Mezey, P. G. *J. Chem. Phys.* **1989**, *90*, 4916–4926.
- (55) Pettersen, E. F.; Goddard, T. D.; Huang, C. C.; Couch, G. S.; Greenblatt, D. M.; Meng, E. C.; Ferrin, T. E. *J. Comput. Chem.* **2004**, *25*, 1605–1612.
- (56) Muhoberac, B.; Wharton, D. *J. Biol. Chem.* **1980**, *255*, 8437–8442.
- (57) Muhoberac, B.; Wharton, D. *J. Biol. Chem.* **1983**, *258*, 3019–3027.
- (58) Cheesman, M. R.; Ferguson, S. J.; Moir, J. W. B.; Richardson, D. J.; Zumft, W. G.; Thomson, A. J. *Biochemistry* **1997**, *36*, 16267–16276.

- (59) Walsh, T. A.; Johnson, M. K.; Greenwood, C.; Barber, D.; Springall, J. P.; Thomson, A. J. *Biochem. J.* **1979**, *177*, 29–39.
- (60) LoBrutto, R.; Wei, Y. H.; Mascarenhas, R.; Scholes, C. P.; King, T. E. *J. Biol. Chem.* **1983**, *258*, 7437–7448.
- (61) Radoul, M.; Centola, F.; Rinaldo, S.; Cutruzzolà, F.; Pecht, I.; Goldfarb, D. *J. Inorg. Chem.* **2009**, *48*, 3913–3915.
- (62) Praneeth, V. V. K.; Nather, C.; Peters, G.; Lehnert, N. *Inorg. Chem.* **2006**, *45*, 2795–2811.
- (63) Serres, R. G.; Grapperhaus, C. A.; Bothe, E.; Bill, E.; Weyhermueller, T.; Neese, F.; Wieghardt, K. *J. Am. Chem. Soc.* **2004**, *126*, 5138–5153.
- (64) Radon, M.; Pierloot, K. *J. Phys. Chem. A* **2008**, *112*, 11824–11832.
- (65) Praneeth, V. V. K.; Neese, F.; Lehnert, N. *Inorg. Chem.* **2005**, *44*, 2570–2572.
- (66) Praneeth, V. V. K.; Nather, C.; Peters, G.; Lehnert, N. *Inorg. Chem.* **2006**, *45*, 2795–2811.
- (67) Blomberg, L. M.; Blomberg, M. R. A.; Siegbahn, P. E. M. *J. Inorg. Biochem.* **2005**, *99*, 949–958.
- (68) Olah, J.; Harvey, J. N. *J. Phys. Chem.* **2009**, *113*, 7338–7345.
- (69) Franke, A.; Stochel, G.; Jung, C.; van Eldik, R. *J. Am. Chem. Soc.* **2004**, *126*, 4181–4191.
- (70) Xu, C.; Spiro, T. G. *J. Biol. Inorg. Chem.* **2008**, *13*, 613–621.
- (71) Neese, F. *J. Chem. Phys.* **2001**, *115*, 11080–11096.
- (72) Neese, F. *Magn. Reson. Chem.* **2004**, *2*, S187–S198.